

Tunable White-Light Emission of Co^{2+} and Mn^{2+} Co-Doped ZnS Nanoparticles by Energy Transfer between Dopant Ions

G. Saavedra-Rodríguez, U. Pal, R. Sánchez-Zeferino, and M. E. Álvarez-Ramos*

Cite This: *J. Phys. Chem. C* 2020, 124, 3857–3866

Read Online

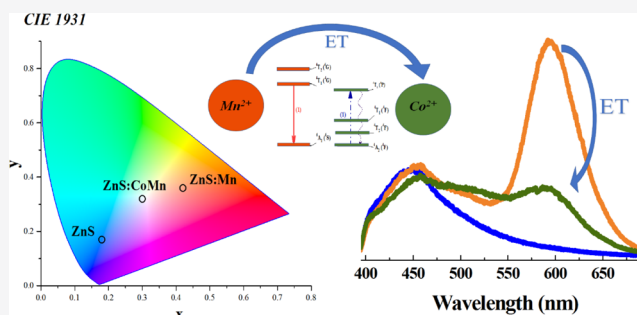
ACCESS |

Metrics & More

Article Recommendations

Supporting Information

ABSTRACT: Fabrication of white light-emitting nanophosphors with high luminous efficacy is an urgent need for the next-generation lighting industry and display systems. While rare-earth ions have been frequently utilized as dopants to fabricate semiconducting and dielectric nanophosphors, the limited abundance of rare-earth elements on our planet demands a search for suitable alternatives. Here, we report the fabrication of ZnS nanoparticles co-doped with Co^{2+} and Mn^{2+} transition metal ions which manifest intense near-white light emission under ultraviolet excitation. While the nanophosphors could be fabricated through a simple low-temperature two-step chemical process, both the color and intensity of their emission can be tuned just by varying the molar concentration of the two dopant ions. The variation of the emission color and its intensity in the nanophosphors due to the dopant ion concentration has been explained considering the interband energy transfer from Mn^{2+} ions to Co^{2+} ions and creation of deep level defect states in the host nanocrystals. The synthesis process utilized in the present work opens up the possibility of fabricating low-cost, emission-tuned, rare-earth-free nanophosphors for developing high-efficiency light-emitting devices.



INTRODUCTION

Semiconductor nanostructures have attracted strong research interest in the last decade because of their superior optical, electrical, and optoelectronic properties. While most of these properties of semiconductor nanostructures can be tuned by controlling their size and morphology, by incorporating a suitable dopant, their electronic band structures can be modified to meet the requirements for specific optoelectronic applications. Optical properties of semiconductor nanostructures of II–VI groups, such as quantum dots and nanoparticles of ZnS, CdS, CdTe, CdSe, ZnTe, and so forth, have been studied extensively for optoelectronic applications,^{1–9} especially for solar cell development and enhancement of the light conversion efficiency of commercial silicon solar cells.^{10–13} They have also been utilized systematically for the fabrication of light-emitting diodes,^{14–20} emitting mainly in the 400–640 nm spectral range, with the possibility of further tuning by controlling their size and impurification.^{8,21,22} While the bandgap energy of these nanostructures can be easily tuned by controlling their size, that is, by taking advantage of the quantum confinement effect, optically stimulated radiative emissions from them could be controlled by metal ion doping. Radiative emissions of semiconductor nanostructures depend generally on the sub-bandgap electronic states, intrinsically generated or through metal ion doping. However, emissions can also occur from the interband transitions of the incorporated atoms or ions of transition metals and rare-earths.^{23–27} Although rare-earth ions are well-known emission

activators for nanophosphors capable of inducing intense emissions in selective spectral regions when incorporated in limited concentrations, they are expensive due to low abundance in the planet.^{28–30}

Most of the II–VI semiconductor nanoparticles and quantum dots without a zinc content exhibit intense photoluminescence (PL) emissions in the 500–640 nm spectral range, that is emitting green to red colors. However, because of the lack of blue emission, they cannot generate white light. For this reason, nanostructured systems based on zinc,^{15,19,21,31,32} especially zinc sulphide (ZnS), have gained strong attention recently. ZnS has intrinsic intrabandgap electronic states, which produce broad blue emission,^{33,34} allowing its tunability for producing emissions in other wavelengths of the visible spectral region. One of the most common ways to modify the optical properties of ZnS nanostructures is through the introduction of dopants or impurities in their crystalline lattice. In fact, Mn^{2+} ions have been systematically incorporated into the ZnS lattice to obtain reddish emission bands.^{25,35,36} Other transition metal ions have also been utilized as dopants for ZnS to improve its emission efficiency. For example, the incorporation of Co^{2+}

Received: November 21, 2019

Revised: January 15, 2020

Published: January 22, 2020

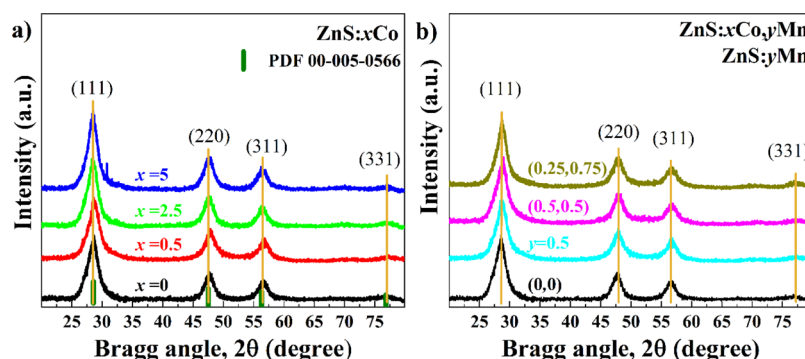


Figure 1. XRD patterns of (a) Co and (b) Mn–Co co-doped ZnS nanoparticles.

ions in low concentrations has been seen to enhance the emission efficiency of ZnS through the creation of defect states inside its energy band gap. However, the incorporation of metal ion dopants in high concentration quenches the emission of ZnS.³⁷

Common synthesis methods utilized to obtain ZnS nanocrystals are the aqueous chemical processes, such as chemical bath deposition, co-precipitation, and solvothermal, using different polymers and capping materials.^{33,38–41} While most of these chemical processes are simple and cost-effective, producing ZnS nanostructures of well-controlled size and morphology along with the introduction of doping ions in a controlled manner remained challenging, due to inherent impurity rejection behavior of small nanostructures.^{42,43} Among the transition metal ions, Co^{2+} and Mn^{2+} have been utilized frequently to impurifying ZnS nanostructures. While the incorporation of Co^{2+} ions in low concentrations has been performed to enhance the intrinsic defect-induced PL emission of ZnS nanostructures,^{44–46} the incorporation of Mn^{2+} ions in ZnS nanostructures as a single dopant has been performed to induce red emission.⁴³ On the other hand, Mn^{2+} and Cu^{2+} ions have been co-doped in ZnS for inducing white light emission.⁴⁴ However, the utilization of Co^{2+} and Mn^{2+} ions as co-dopants to tune the emission behavior of ZnS nanostructures has not been reported in the literature.

In this article, we present the synthesis of well-dispersed ZnS nanoparticles of 4–4.5 nm size range, co-doped with Co^{2+} and Mn^{2+} ions, and their room-temperature PL emission behaviors. The well-crystalline semiconductor nanoparticles were synthesized by a combined co-precipitation–hydrothermal method and characterized by X-ray diffraction (XRD), transmission electron microscopy (TEM), diffuse reflectance spectroscopy (DRS), Raman spectroscopy, and room-temperature PL spectroscopy. By adjusting the concentration of incorporated Co^{2+} and Mn^{2+} ions, PL emissions of the nanoparticles could be tuned to the visible spectral range, which is very important for their utilization in white light-emitting display devices. The mechanisms of emission tuning in the co-doped ZnS nanoparticles have been discussed.

EXPERIMENTAL DETAILS

Zinc nitrate hexahydrate ($\text{Zn}(\text{NO}_3)_2 \cdot 6\text{H}_2\text{O}$, >98%), sodium sulfide nonahydrate ($\text{Na}_2\text{S} \cdot 9\text{H}_2\text{O}$, ≥98%), cobalt nitrate hexahydrate ($\text{Co}(\text{NO}_3)_2 \cdot 6\text{H}_2\text{O}$, >98%), manganese nitrate tetrahydrate ($\text{Mn}(\text{NO}_3)_2 \cdot 4\text{H}_2\text{O}$, >98%), and cetyltrimethylammonium bromide (CTAB), all of analytical grade, were purchased from Sigma-Aldrich, Mexico, and used as received, without further processing. Deionized (DI) water from a Milli

Q system was used as a solvent for reactions, as well as for washing the materials.

The doped and undoped ZnS nanoparticles were synthesized using a combined co-precipitation–hydrothermal process. First, small ZnS clusters (doped and undoped) were prepared by co-precipitation at 4–6 °C temperature. Then, the amorphous ZnS clusters (doped and undoped) were treated hydrothermally for their further growth and crystallization. For the co-precipitation of ZnS clusters, 12.5 mL of 0.5 M aqueous zinc nitrate solution was mixed with 12.5 mL of 0.5 M solution of sodium sulfide under magnetic agitation. A 0.5 M aqueous solution of cobalt nitrate hexahydrate and/or manganese nitrate tetrahydrate was added to the earlier mixture in different volumes to maintain the desired concentration of Co^{2+} and/or Mn^{2+} ions in the reaction mixture. Several mixtures containing nominal 0.5, 2.5, 5, and 10 mol % of cobalt nitrate, 0.5 and 1.0 mol % of manganese nitrate, and Co/Mn nitrates in 0.5/0.5 and 0.25/0.75 molar ratios were prepared. The mixtures were transferred to a cold bath under magnetic agitation, maintaining its temperature in-between 4 and 6 °C. After 1 h of reaction, the mixtures become turbid white, indicating the formation of ZnS clusters.

In the second step, about 250 mg of CTAB was dissolved into each of the earlier reaction mixtures and transferred to Teflon-lined stainless-steel autoclaves (40 mL capacity). The autoclaves were then sealed and heated in a gravity furnace at 140 °C for 8 h. The reaction products were collected by centrifugation, washed several times with DI water and ethanol, and dried at 80 °C for 5 h, obtaining white powders.

The doped and undoped ZnS nanoparticles obtained by the procedure described above were characterized to study their morphology, crystalline structure, and optical properties. The structural analysis of the samples was carried out in a Bruker D8 Discover X-ray diffractometer (XRD) utilizing $\text{Cu K}\alpha$ radiation ($\lambda = 1.5046 \text{ \AA}$) in 10–80° 2θ range, at a scan speed of 2°/min in 0.02° steps. For morphology and fine-structure analysis, low- and high-resolution TEM images of the samples were recorded in a JEOL JEM-2010F microscope operating at 200 kV. For TEM analysis, the powders were suspended in ethanol (0.1 mg/mL) and left to dry on a carbon-coated copper grid after drop casting. Room-temperature Raman spectra of the samples were recorded in a HORIBA LabRam 800 spectrometer, using a He-Ne laser ($\lambda = 632.8 \text{ nm}$) as the excitation source and a thermoelectrically cooled charge-coupled device detector.

Optical properties of the synthesized nanoparticles (doped and undoped ZnS) were studied by DRS and PL spectroscopy. DRS spectra of the samples were recorded in an Agilent Cary

Table 1. Lattice Strain and Structure Parameters of the Fabricated Nanocrystals Extracted from Their XRD Patterns

sample	plane	fwhm (rad)	av. crystallite size (nm)	cell parameter (Å)	strain
ZnS	(111)	0.0384	4.2	5.42	5.3
ZnS:0.5Co	(111)	0.0389	3.7	5.38	6.7
ZnS:2.5Co	(111)	0.0362	4.3	5.43	5.3
ZnS:5Co	(111)	0.0342	4.3	5.43	2.7
ZnS:0.5Mn	(111)	0.0394	3.7	5.37	6.7
ZnS:0.5Co0.5Mn	(111)	0.0407	3.6	5.36	5.7
ZnS:0.25Co0.75Mn	(111)	0.0358	4.0	5.39	2.4

5000 UV–vis spectrophotometer coupled with a hemispherical integrating sphere. For band gap energy estimation, the recorded DRS spectra were processed with Kubelka–Munk treatment. Room-temperature PL spectra of the samples were recorded in a HORIBA iHR-320 spectrofluorometer, utilizing a 1200/500 grating and ambient-cooled Hamamatsu R928 multi-alkali photomultiplier tube as a detector. Emissions from a 450 W Xe arc lamp and a 325 nm He–Cd laser line with the maximum incident power of 5 mW were utilized for sample excitation. Room-temperature time-resolved fluorescence spectra of the samples were recorded in a Jobin Yvon Triax-550 monochromator coupled with a HORIBA Jobin Yvon i-Spectrum Two ICCD detector, using an Opolette HE 355 LD + UVDM pulsed laser of 10 ns pulse duration, as an excitation source.

RESULTS AND DISCUSSION

In order to evaluate the crystallinity and structural phase of the synthesized nanostructures, their room-temperature XRD spectra were recorded in the 20–80 2θ range (Figure 1). The appearance of well-defined diffraction peaks in the XRD patterns of the samples indicates their good crystallinity. All the samples (doped and undoped) revealed four diffraction peaks at around 28.5, 47.7, 56.6, and 77.3°, which correspond to the (111), (220), (311) and (331) planes of ZnS in the face-centred cubic (fcc) phase (PDF # 005-0566). The average crystallite size in the nanostructures was estimated using Debye–Scherrer relation⁴⁷ considering the main diffraction peak (111) in their XRD patterns

$$D = \frac{K\lambda}{\beta \cos(\theta)} \quad (1)$$

where D is the average diameter of the crystallite in the direction perpendicular to the planes associated to the selected peak, K is the shape-factor parameter, which is 0.94 for spheroidal shaped particles of the cubic structure, λ is the excitation wavelength ($\lambda = 1.5046$ Å), and β is the full width at the half maximum (fwhm) of the selected peak. A pseudoVoigt function fitting was carried out to the principal diffraction peak (111) using 0.94 as a shape factor to estimate its fwhm values for different samples. The estimated average crystallite size values obtained for the samples are presented in Table 1.

Using Bragg's relation (eq 2) and interplanar spacing d (eq 3) for the most prominent reflection, we estimated the lattice parameter " a " of the nanocrystals to monitor the effect of Co^{2+} and Mn^{2+} ion incorporation in their lattice. Lattice strain (ϵ) induced by the incorporation of the dopants was also estimated using the Williamson–Hall⁴⁸ relation (eq 4)

$$n\lambda = 2d \sin \theta \quad (2)$$

$$d_{hkl} = a/\sqrt{h^2 + k^2 + l^2} \quad (3)$$

$$\beta_{hkl} \cos \theta = \left(\frac{k\lambda}{D} \right) + 4\epsilon \sin \theta \quad (4)$$

The estimated average grain size, lattice parameter, and lattice strain for the doped and undoped nanocrystals are listed in Table 1. As can be seen in Table 1, although the lattice strain in the nanocrystals reduces significantly with the incorporation of Co^{2+} and/or Mn^{2+} ions, variations in the crystallite size and lattice parameter did not reveal any particular trend. While the results confirm the incorporation of Co^{2+} and/or Mn^{2+} ions in the ZnS lattice, their concentrations in the nanostructures were low, probably due to the small sizes of the nanocrystals.

As the ionic radius of Co^{2+} (79 pm) is smaller than the ionic radius of Zn^{2+} (88 pm), they have a good possibility to be accommodated at Zn^{2+} sites of the ZnS lattice through substitution. On the other hand, Mn^{2+} ions with ionic radius (97 pm) is about 10% bigger than that of Zn^{2+} and hence can be accommodated both at the Zn^{2+} sites and at interstitial spaces.

As the lattice constant of the ZnS nanoparticles did not suffer significant change due to Co^{2+} and/or Mn^{2+} doping, probably most of the dopant atoms incorporated at the interstitial sites of the ZnS lattice, creating zinc vacancies in the nearest cationic sites for charge compensation.

Doping concentration limits and solubility of metal ions in semiconductor nanostructures are closely related to the chemical potential of the host constituents and the formation energy of the dopant ion compounds⁴⁹ and therefore are strongly size-dependent. While a reduction of particle size is known to reduce its dopant solubility,^{42,43,50} an increase in the nominal concentration of dopants might have caused a competition between the substitution and interstitial accommodation of dopant ions, resulting in a higher structural modification at lower doping concentrations.

TEM both at low and high resolution (HRTEM) was carried out to evaluate the size and crystallinity of the ZnS nanoparticles. As can be noticed in the TEM micrograph presented in Figure 2a,b, the undoped sample consists of quasi-spherical particles smaller than 10 nm. The HRTEM images of the sample presented in Figure 2c,d revealed most of the particles are of about 4.0 nm size and are of highly crystalline nature. In fact, the size distribution histogram constructed by measuring the size of more than 200 nanoparticles from their HRTEM images (Figure 2e) revealed their average size of about 4.2 nm. The appearance of clear lattice fringes in the HRTEM images of the nanoparticles (Figure 2d) clearly demonstrates their good crystallinity.

In addition to the particle size analysis, an inspection of HRTEM images was performed to confirm the type of the crystal structure of the sample, determined by XRD, by measuring the interplanar distances. Figure 2d shows a

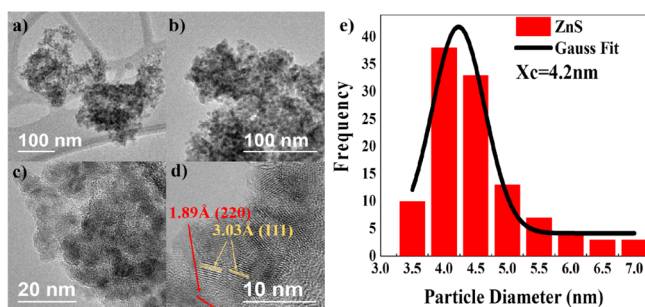


Figure 2. TEM and HRTEM micrographs of undoped ZnS nanostructures. The micrographs presented in (a–c) with gradually increased magnification clearly reveal their good dispersion. The HRTEM image presented in (d) shows their good crystallinity. Size distribution histogram constructed by measuring the size of individual particles is presented in (e).

representative HRTEM micrograph that exhibits interplanar distances of 3.03 and 1.89 Å, on average, corresponding to (111) and (220) planes respectively, corresponding to an fcc structure of ZnS (zinc blende, PDF #00-05-0566).

Similar TEM and HRTEM studies were performed on the ZnS:Co (0.5 and 2.5 mol % nominal Co concentrations), ZnS:Mn (0.5 mol % nominal Mn concentration), and ZnS:CoMn (0.5, 0.5 mol % nominal concentration) nanostructures (Figure 3). TEM micrographs of all the nanostructures revealed their quasi-spherical shape, with an average size of around 4.0 nm. As can be noticed in their size distribution histograms (at the right side of the corresponding micrograph), the average diameter of the particles does not vary significantly with doping.

Raman spectra were recorded on the doped and undoped ZnS nanostructures to study their structural characteristics further. All the samples revealed characteristic vibrational modes of zinc sulphide in the cubic phase.^{51,52} In general, the Raman signals of the samples are broad and of moderate intensity, probably due to smaller size of nanocrystals. The most prominent dispersion peaks appeared around 264 and 345 cm^{-1} correspond to $E_1(\text{TO})$ and $E_1(\text{LO})$ phonons of ZnS, respectively. Other bands appeared with lower intensity are either higher orders of the fundamental vibrations or of multiphononic nature. The weak bands appeared around 145, 308, and 430 cm^{-1} for the undoped ZnS nanostructures correspond to multiphononic vibrations $2E_2^1$, E_2^2 , and $E_1(\text{TO}) + 2E_2^1$, respectively. In the case of Co^{2+} impurities, a weak band centered around 308 cm^{-1} appeared, which corresponds to the silent mode E_2^2 (Figure 4a).^{51–53} As can be observed, the incorporation of Co^{2+} ions in lower concentrations does not affect much the spectral features of ZnS nanostructures. The major change observed for Co^{2+} doped nanostructures is the absence of the 430 cm^{-1} multiphonon mode for higher concentrations. For the highest Co^{2+} concentration, that is, for the ZnS:10Co nanostructures, the intensity of the $E_1(\text{TO})$ signal reduced with respect to the intensity of the $E_1(\text{LO})$ signal. Also, the band becomes considerably broad. This change in the peak shape is probably due to the formation of CoS_x , which also exhibits a strong Raman signal in the 320–380 cm^{-1} range.⁵⁴ As can be seen in Figure 4b,c, the Mn^{2+} doped ZnS nanostructures also revealed fundamental $E_1(\text{TO})$ and $E_1(\text{LO})$ vibrational modes of cubic ZnS. The silent mode E_2^2 also occurred as in case of the samples prepared with low concentration Co^{2+} doping. However, the co-doped nano-

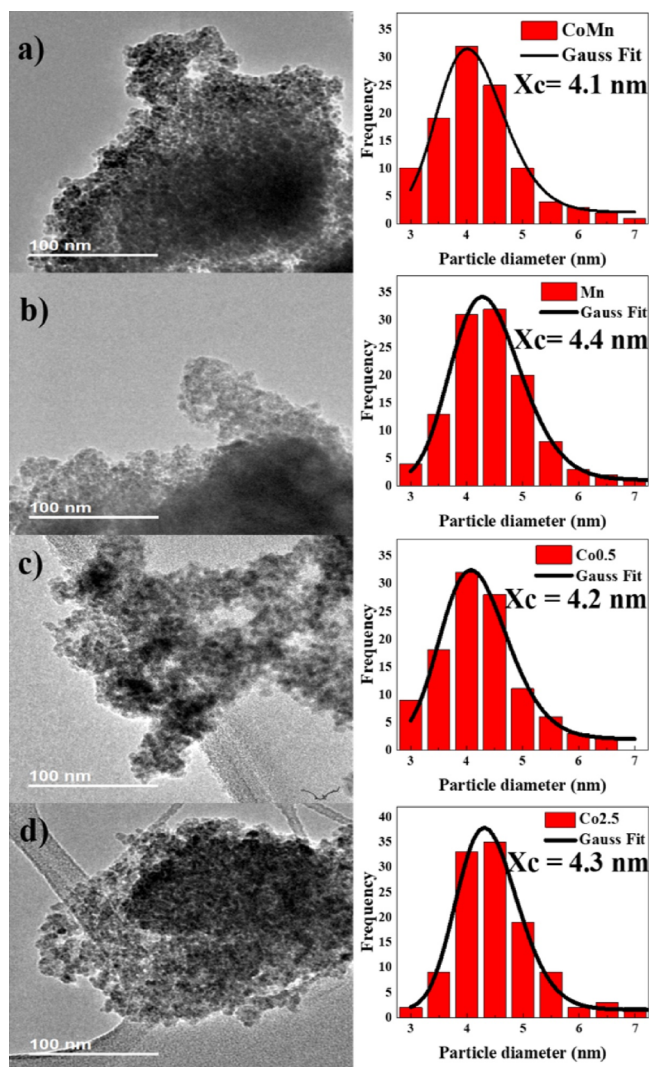


Figure 3. Typical TEM micrographs and size distribution histograms of (a) ZnS:0.5Co0.5Mn, (b) ZnS:0.5Mn, (c) ZnS:0.5Co, and (d) ZnS:2.5Co samples.

structures revealed very little change in the intensity and position of the fundamental vibrational modes of ZnS (Figure 4c), indicating minimum distortion of the host ZnS lattice.

Variation of optical properties, specifically, the band gap energy of ZnS nanoparticles on the incorporation of Co^{2+} and Mn^{2+} ions was analyzed by recording DRS spectra of the powder samples in the UV–vis spectral range. To estimate the band gap energy, Kubelka–Munk (K–M) treatment⁵⁵ was performed on the recorded DRS spectra. For a direct band semiconductor, the optical band gap is related to its wavelength-dependent absorption coefficient, following the relation

$$\alpha h\nu = C_1(h\nu - E_g)^{1/2} \quad (5)$$

When the light is dispersed in a diffuse manner, the absorption coefficient α of a material is related with the K–M absorption coefficient by $K = 2\alpha$, for a specific wavelength of the incident light. Assuming the dispersion coefficient (S) does not depend on the wavelength, the K–M relation can be rewritten as

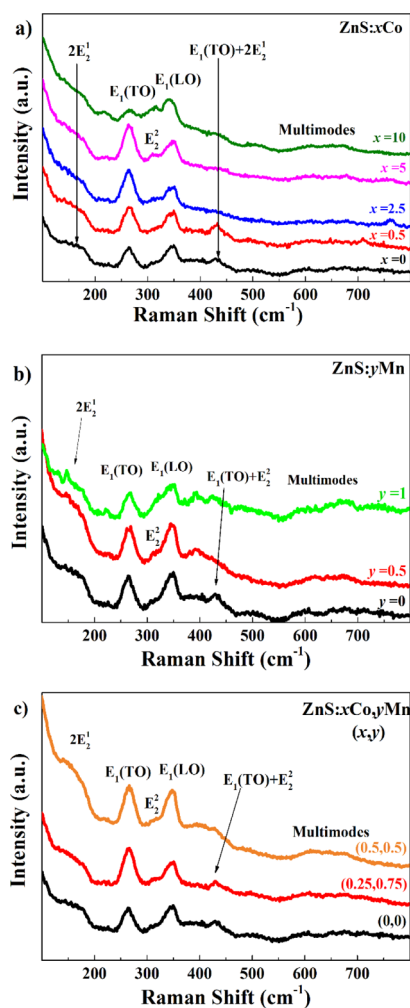


Figure 4. Raman spectra of (a) Co^{2+} , (b) Mn^{2+} , and (c) $\text{Co}^{2+}/\text{Mn}^{2+}$ co-doped ZnS nanoparticles. All the principal vibrational modes correspond to the cubic ZnS lattice.

$$\frac{K}{S} = \frac{(1 - R_\infty)^2}{2R_\infty} \equiv F(R_\infty) \quad (6)$$

where $R_\infty = R_{\text{sample}}/R_{\text{standard}}$ whose values oscillate between 0 and 1. From eqs 5 and 6, we get the expression

$$[F(R_\infty)h\nu]^2 = C_2(h\nu - E_g) \quad (7)$$

By plotting $[F(R_\infty)h\nu]^2$ against photon energy ($h\nu$), and extrapolation of the linear regime to the photon energy axis, we determined the optical band gap energy (E_g) values of the doped and undoped ZnS nanostructures,⁵⁵ as shown in Figure 5b,d.

As can be noticed (Figure 5b,d), there exists no specific trend of band gap energy variation of ZnS nanoparticles due to Co^{2+} and/or Mn^{2+} doping. While the variations are nominal, E_g variation of the doped ZnS nanoparticles follows the same trend as their lattice parameter values estimated from XRD analysis (Table 1). A maximum increase in the band gap energy of 0.06 eV was observed for the nanoparticles with the lowest nominal cobalt content (ZnS:0.5Co, Figure 5b), probably due to their higher lattice strain (Table 1). On the other hand, no noticeable variation in E_g could be detected due to Mn^{2+} doping. A small but significant increase in E_g could be

detected only for the ZnS nanoparticles co-doped with Mn and Co ions (Figure 5d).

A careful observation on the DRS spectra presented in Figure 5a,c would reveal that the cobalt doped and co-doped samples exhibit an absorption band in the 640–800 nm region, not revealed by the undoped or Mn^{2+} -incorporated ZnS nanostructures. To analyze this behavior, the absorption spectra of the samples in this spectral range are presented in Figure 6a. As can be noticed, all the samples manifest broad absorption in the 640–800 nm spectral range, with three well-defined components. While the absorption corresponds to the interband transition ${}^4\text{A}_2({}^4\text{F}) \rightarrow {}^4\text{T}_1({}^4\text{P})$ of Co^{2+} ions (Figure 6b), its triplet structure is associated to the polarization splitting of the “3d” orbitals for tetrahedrally coordinated Co^{2+} ions; that is, the triple degeneracy of the excited state is broken by the influence of the closest ion neighbors because of the orbital orientation with respect to the crystal lattice.^{56–58}

To study the effect of Co^{2+} and Mn^{2+} ion incorporation on the emission behavior of ZnS nanoparticles, the PL spectra of the undoped and doped samples were recorded at room temperature, by exciting the samples with a 325 nm He-Cd laser (Figure 7). As can be seen, the emission spectra of the undoped and Co-doped ZnS nanoparticles reveal a broad emission extending from 360 to 600 nm, with a maximum around 450 nm. This broad emission in ZnS nanostructures has been frequently associated to deep and shallow defect states associated to sulfur (V_S) and zinc (V_{Zn}) vacancies in ZnS, whose deconvolution (400, 444, 500, and 570 nm emission components) is presented in the inset of Figure 7a.³³ It should be noted that the intensity of this emission is enhanced for the lowest Co^{2+} concentration (sample ZnS:0.5Co), probably due to the introduction of shallow electronic states in the ZnS band gap. However, with the increase of Co^{2+} concentration (nominal), the intensity of the emission decreased drastically. The observed reduction of emission intensity can be associated to the non-radiative transitions between the interband states of Co^{2+} ions,^{56,59} as illustrated in Figure 9b. On the other hand, incorporated Co^{2+} ions can also form CoS_x , which have emission bands in the same spectral range,⁵⁴ modifying the shape of the emission band of the Co-doped ZnS nanoparticles.

Figure 7b depicts the PL spectra of Mn^{2+} doped and $\text{Co}^{2+}/\text{Mn}^{2+}$ co-doped ZnS nanoparticles. As can be seen, Mn^{2+} -doped ZnS nanostructures reveal wider emission features containing two intense emission bands. The blue emission band centered around 450 nm corresponds to ZnS nanostructures (as discussed earlier). The intensity of this emission band increases gradually with the increase of Mn^{2+} concentration contrary to the change noted for Co^{2+} doping. The other, relatively sharper emission band appeared around 600 nm, is associated to ${}^4\text{T}_1(\text{G}) \rightarrow {}^6\text{A}_1(\text{S})$ interband transition of Mn^{2+} ions.^{26,35,36,60} In most cases, the intensity of Mn^{2+} emissions exceeds the intensity of the emission from the host material,⁶¹ making it difficult to have both contributions: the blue emission plus the red emission at a same intensity order, for optical applications. In order to avoid this problem, a double-doping (co-doping) was carried out varying the $\text{Co}^{2+}/\text{Mn}^{2+}$ ratio in the host ZnS nanostructures. Following the same procedure, ZnS nanoparticles were synthesized with Co^{2+} and Mn^{2+} co-doping, maintaining the nominal $\text{Co}^{2+}/\text{Mn}^{2+}$ molar ratio 1:3 and 1:1. The nanostructures were denominated as ZnS:0.25Co0.75Mn and ZnS:0.5Co0.5Mn. The emission spectra of the doped and undoped samples were evaluated

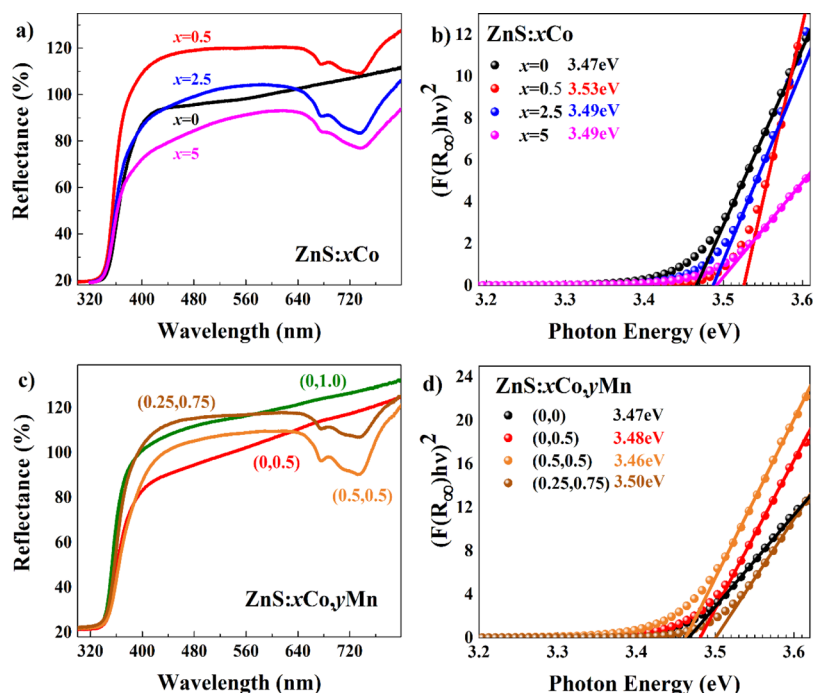


Figure 5. DRS spectra of the doped and undoped ZnS (a,c) nanostructures and corresponding Kubelka–Munk plots (b,d).

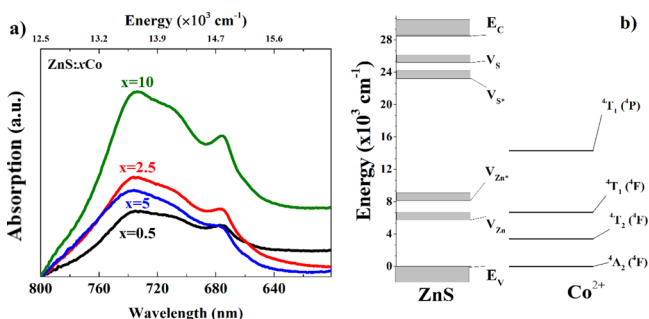


Figure 6. Optical absorption spectra of the co-doped ZnS nanoparticles (a) in the vis–NIR spectral range and (b) band diagram of ZnS energy states and interband energy levels of Co²⁺ ions.

with respect to the tristimulus response of human eyes, established by CIE 1931 standard to obtain their chromaticity coordinates. The results are presented in Figure 7c, which indicates that all the nanophosphors do not emit white light under 325 nm excitation.

Room-temperature PL measurements were also carried out on the doped and undoped nanostructures at lower energy excitations, utilizing 350 and 370 nm emissions of a Xe arc-lamp (Figure 8a,b) to promote transitions between different near-band trap levels associated to intrinsic defects of ZnS³³ and interband transitions of the dopant ions, as can be noticed in Supporting Information Figures S1 and S2, in which the deconvoluted spectra corresponding to doped and undoped samples are presented. The spectra are composed of multiple bands corresponding to $V_s \rightarrow E_v$, $E_g \rightarrow V_{Zn}$, $V_{Eg} \rightarrow V_{Zn^*}$, $V_{S^*} \rightarrow V_{Zn}$, $V_{S^*} \rightarrow V_{Zn^*}$ (396–400, 444, 500, 570, and 630 nm) transitions of the host intrinsic defect levels, and the ${}^4T_1({}^4G) \rightarrow {}^6A_1({}^6S)$ of the Mn²⁺ ions (595 nm). CIE 1931 chromaticity calculations were performed, and the results are plotted in Figure 8c,d. Under 350 nm excitation, the Co²⁺ and Mn²⁺ co-doped ZnS nanoparticles exhibit the blue emission of the ZnS host (as discussed earlier), along with the interband emissions

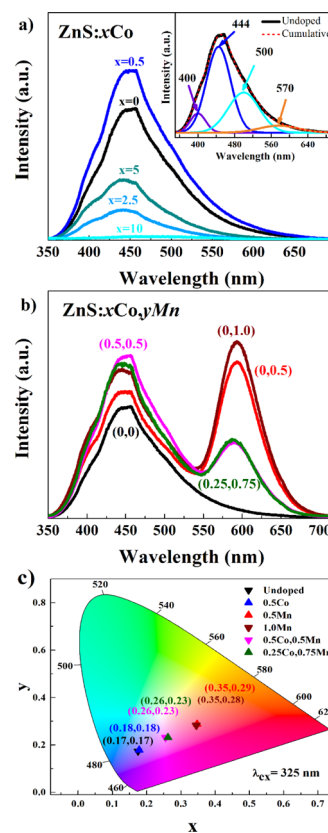


Figure 7. Room-temperature PL spectra of the (a) Co²⁺ doped and (b) Mn²⁺ and Co²⁺/Mn²⁺ co-doped ZnS nanoparticles under 325 nm laser excitation. (c) Chromaticity diagram of the doped and undoped ZnS nanoparticles.

of Mn²⁺ ions around 595 nm and defect emission around 500 nm. On the other hand, under 370 nm excitation, the host emission band near 400 nm decreases, but the 500 nm band

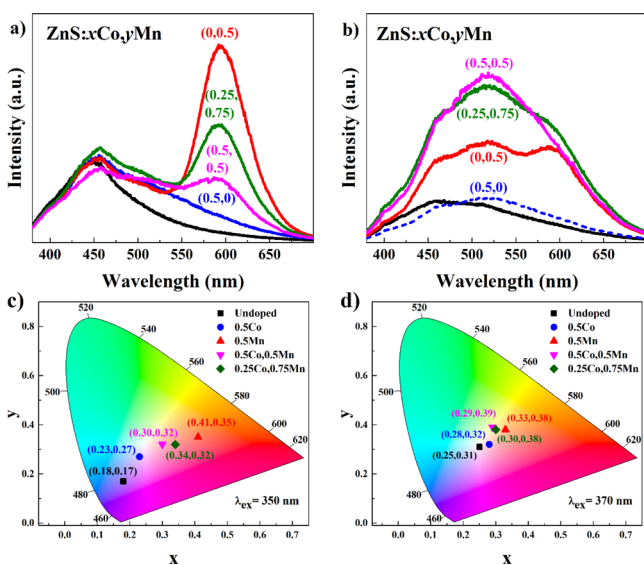


Figure 8. Room-temperature PL spectra of ZnS and ZnS:CoMn samples under Xe lamp excitation at (a) $\lambda = 350$ nm and (b) $\lambda = 370$ nm (b). (c,d) Corresponding CIE1931 chromaticity coordinates.

exhibits a clear enhancement with respect to the higher energy excitations. Moreover, the intensity of the red emission associated with Mn^{2+} ions decreases.

As can be noticed (Figure 8c), the emission of the co-doped sample with nominal $\text{Co}^{2+}/\text{Mn}^{2+}$ ion ratio 1:1 and chromaticity coordinates (0.30,0.32) is very close to the perfect white (0.33,0.33) coordinate in the chromaticity diagram, when excited by 350 nm light (from Xe lamp). This phenomenon can be explained by considering the effect of excitation energy and the contribution of energy transfer processes in the $\text{Co}^{2+}/\text{Mn}^{2+}$ co-doped ZnS nanostructures. A higher energy of excitation (e.g. 325 nm laser excitation) promotes the radiative transitions associated to band-to-band transition, that is, from the conduction band to the valence band, and the transitions from high energy defect (HD) states to lower energy defect (LD) states of ZnS energy band. On the other hand, lower energy excitations (e.g. 350 and 370 nm excitations from Xe lamp) promote transitions from the HD states to LD states, for all the doped and undoped ZnS nanostructures.

The emission behavior of the doped nanostructures also depends critically on the guest–host combination. As has been evidenced by the results presented above, nonradiative energy transfer from Mn^{2+} to Co^{2+} occurs in the co-doped nanostructures, generating the possibility of emission tuning through the manipulation of doping the ion ratio in the host lattice, along with the adjustment in the energy of exciting radiation (Figures 7c and 8c,d). The energy transfer process has been discussed in detail in the following subsection.

In order to explain the observed (Figures 7b and 8a) emission tuning of doped ZnS nanoparticles through intensity modulation of Mn^{2+} ion interband emission by the introduction of Co^{2+} ions, it was necessary to study if an energy transfer process occurs from Mn^{2+} to Co^{2+} ions,^{37,62,63} which allows us to control the emission intensity of the nanophosphor by varying the nominal concentration of the two dopants. As can be seen in Figure 9a, the interband emission of Mn^{2+} ion and interband absorption of Co^{2+} ion overlap each other, which is the principal criterion for the

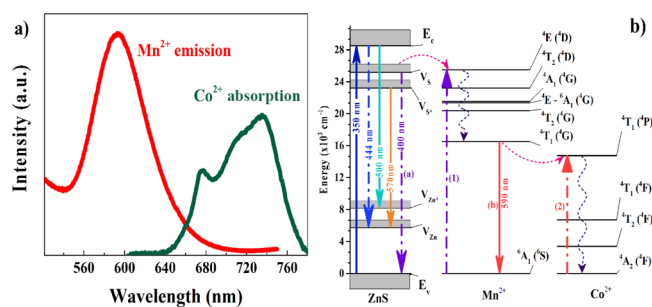
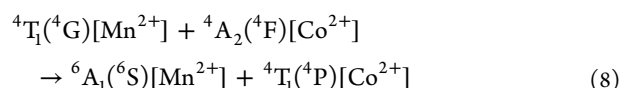


Figure 9. (a) Room-temperature emission spectrum of Mn^{2+} ions (in ZnS:0.5Mn sample, under 350 nm excitation) and absorption spectrum of Co^{2+} ions (in ZnS:0.5Co sample), and (b) electronic transitions between the intrinsic defects of the host, excitation mechanism of the Mn^{2+} ions (a) \rightarrow (1) and possible energy transfer process between Mn^{2+} and Co^{2+} ions (b) \rightarrow (2).

energy transfer process between the two ions. The energy transfer between the two ions occurs possibly through the transitions



The details of the energy transfer process have been schematically presented in Figure 9b, in which the energy of the relaxation (a) $V_S \rightarrow E_v$ is equivalent to the absorption (1) ${}^6A_1({}^6S) \rightarrow {}^4E({}^4D)$ of the Mn^{2+} ions, and the Mn^{2+} relaxation (b) ${}^4T_1({}^4G) \rightarrow {}^6A_1({}^6S)$ and the absorption (2) ${}^4A_2({}^4F) \rightarrow {}^4T_1({}^4P)$ of Co^{2+} are in the same order of energy; in this way, (a) \rightarrow (1) represents the mechanism of excitation of the Mn^{2+} ions, and (b) \rightarrow (2) represents the possible mechanism of the energy transfer between Mn^{2+} and Co^{2+} .

For a better understanding of the Mn^{2+} to Co^{2+} energy transfer process, the decay profiles of Mn^{2+} ion emission in the singly doped ZnS (ZnS:0.5Mn) and double doped samples (ZnS:0.25Co0.75Mn and ZnS:0.5Co0.5Mn) were recorded at the room temperature. Figure 10 presents the time-resolved decay profiles of 595 nm emission of Mn^{2+} ions upon 350 nm excitation.

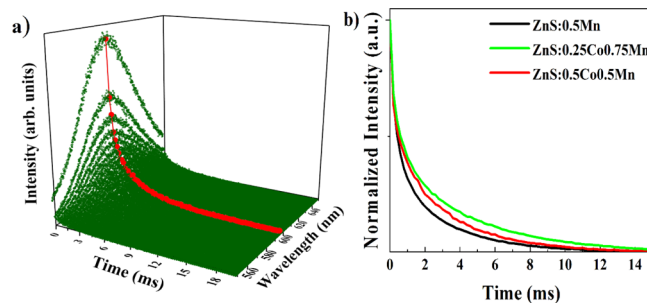


Figure 10. Room-temperature time resolved fluorescence of ZnS:0.5Mn sample (a) and decay profiles of ZnS nanoparticles doped with different ratios of Co^{2+} and Mn^{2+} ions (b).

Because of the nonexponential evolution of the Mn^{2+} emissions, the average lifetimes were calculated utilizing the relation⁶⁴

$$\tau = \frac{\int I(t) dt}{\int I(t) t dt} \quad (9)$$

where t is the time and $I(t)$ is the time dependence of the intensity. The average decay times of the emission were estimated to be 4.68, 4.52, and 4.38 ms, in the single-doped ZnS:0.5Mn, co-doped ZnS:0.25Co0.75Mn samples, and co-doped ZnS:0.5Co0.5Mn samples, respectively. The shorter decay time for the co-doped samples is due to a non-radiative energy transfer from Mn^{2+} to Co^{2+} . The η and P_{MC} efficiency and probability of the energy transfer respectively, could be estimated using the relation⁶⁵

$$\eta = 1 - \frac{\tau_{\text{MC}}}{\tau_{\text{M}}} \quad (10)$$

$$P_{\text{Mn} \rightarrow \text{Co}} = \frac{1}{\tau_{(\text{MC})}} - \frac{1}{\tau_{\text{M}}} \quad (11)$$

where τ_{MC} is the average lifetime of the co-doped sample and τ_{M} is the average lifetime of the singly doped sample. The efficiencies and probabilities values of the energy transfer are listed in Table 2, which indicates $\text{Mn}^{2+} \rightarrow \text{Co}^{2+}$ is more probable for the ZnS:0.5CoMn0.5 sample.

Table 2. Estimated Carrier Lifetime in Mn^{2+} and $\text{Co}^{2+}/\text{Mn}^{2+}$ Co-Doped ZnS Nanoparticles

sample	τ (ms)	η	P_{MC}	γ_{10}
ZnS:0.5Mn	4.68			
ZnS:0.25Co0.75Mn	4.52	0.03	7.97	0.61
ZnS:0.5Co0.5Mn	4.38	0.06	14.67	0.70

To analyze the main mechanism through which the energy transfer occurs, the time profile of the co-doped samples was fitted to the Inokuti and Hirayama model (H–I) for the ${}^4\text{T}_1(4\text{G}) \rightarrow {}^6\text{A}_1(6\text{S})$ emission of Mn^{2+} at 595 nm. This model describes the process of energy transfer from donor to acceptor ions, taking into consideration that it is much faster than the energy diffusion among donor ions. For multipolar interaction, the temporal dependence of the Mn^{2+} emission can be fitted using the relation^{65,66}

$$I(t) = I_0 e^{(-t/\tau_{\text{M}} - \gamma_{\text{S}} t^{3/S})} \quad (12)$$

where I_0 is the intensity at $t = 0$, τ_{M} is the donor (Mn^{2+}) lifetime in the absence of acceptors (Co^{2+}), γ_{S} is a measure of the direct energy transfer, and S is the multipolar interaction parameter. The value of the S parameter is related with the dipole–dipole, dipole–quadrupole, and quadrupole–quadrupole interactions, for $S = 6, 8,$ and 10 , respectively; the best fitting of the time profile spectrum varying the S value indicates the dominant multipole interaction. For both the co-doped samples (Figure 11) ZnS:0.25Co0.75Mn and ZnS:0.5Co0.5Mn, the best fitting was obtained for $S = 10$ with $\gamma_{10} = 0.61 \text{ s}^{-1/2}$ and $\gamma_{10} = 0.70 \text{ s}^{-1/2}$. The low efficiency with which the nonradiative energy transfer $\text{Mn}^{2+} \rightarrow \text{Co}^{2+}$ occurs is consistent with the result that the dominant mechanism of interaction through which this energy transfer occurs is by means of a quadrupole–quadrupole type.

The singly Mn^{2+} ion doped ZnS nanoparticles revealed a characteristic recombination lifetime of $\tau_{\text{M}} = 4.68$ ms. As can be noticed, the value of the lifetime changes on incorporating Co^{2+} ions. While a change in the carrier lifetime of the interband emission of Mn^{2+} ions into the co-doped nanophosphor evidences the energy transfer process between the two dopant ions, its variation with Co^{2+} ion concentration in

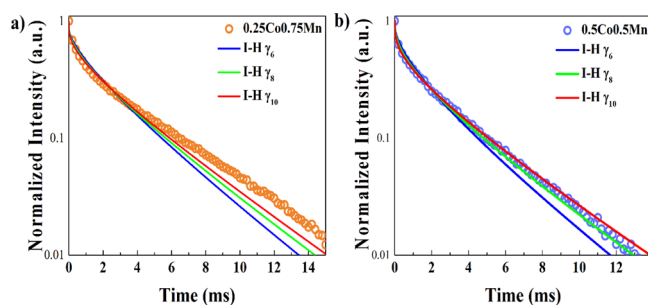


Figure 11. Room-temperature PL decay profiles fitting with the Inokuti and Hirayama model (I–H) of ZnS nanoparticles doped with different ratios of Co^{2+} and Mn^{2+} ions, 1:3 (a) and 1:1 (b), showing the variation of the S parameter.

the nanocrystals is due to the introduction of higher number of defect states into the energy band gap of the host structure, producing changes in the ion–host interactions.^{62,66} The emission behaviors displayed by the fabricated nanophosphors indicate that ZnS:0.5Mn and ZnS:0.5Co0.5Mn nanoparticles can be utilized as warm and cold white light emitters, respectively, under 350 nm UV excitation.

CONCLUSIONS

Through a combined co-precipitation–hydrothermal process, we could synthesis small (4 nm size), well-dispersed ZnS nanoparticles of good crystallinity. Transition metal ions such as Mn^{2+} and Co^{2+} of different nominal mol % could be incorporated to tune the emission behavior of the nanocrystals. While the undoped ZnS nanoparticles exhibit their intrinsic defect emission in the blue spectral region, incorporation of Co^{2+} ions enhances the emission, creating deep level defect states in their energy band gap. Incorporation of Mn^{2+} ions induces red emission to the nanostructures associated to ${}^4\text{T}_1(4\text{G}) \rightarrow {}^6\text{A}_1(6\text{S})$ interband transition. The red emission of the Mn^{2+} ion doped ZnS nanocrystals could be modulated by Co^{2+} ion co-doping, taking advantage of the energy transfer from Mn^{2+} to Co^{2+} ions. By controlling the molar concentrations of Co^{2+} and Mn^{2+} ions, the emission characteristics of the co-doped ZnS nanocrystals could be tuned to emit in the visible spectral region. Because of intense PL emission in the visible spectral region, the synthesized nanostructures can be utilized as white emitting phosphors to fabricate display devices.

ASSOCIATED CONTENT

Supporting Information

The Supporting Information is available free of charge at <https://pubs.acs.org/doi/10.1021/acs.jpcc.9b10890>.

Deconvolution of PL spectra corresponding to doped and undoped ZnS nanoparticles under 350 and 370 nm UV excitation and the components of each deconvoluted spectrum are associated to transitions between defect levels of the ZnS structure and interatomic levels of dopants, depicted in the energy diagram of each figure (PDF)

AUTHOR INFORMATION

Corresponding Author

M. E. Álvarez-Ramos – Departamento de Física, Universidad de Sonora, 83000 Hermosillo, Mexico; orcid.org/0000-0001-7598-9683; Email: mario@alvarez.unison.mx

Authors

G. Saavedra-Rodríguez – Departamento de Física, Universidad de Sonora, 83000 Hermosillo, Mexico; orcid.org/0000-0002-6608-787X

U. Pal – Instituto de Física, Benemérita Universidad Autónoma de Puebla, 72570 Puebla, Mexico; orcid.org/0000-0002-5665-106X

R. Sánchez-Zeferino – Departamento de Física, Universidad de Sonora, 83000 Hermosillo, Mexico; orcid.org/0000-0002-1256-6836

Complete contact information is available at:
<https://pubs.acs.org/10.1021/acs.jpcc.9b10890>

Notes

The authors declare no competing financial interest.

ACKNOWLEDGMENTS

G. Saavedra would like to thank Consejo Nacional de Ciencia y Tecnología (CONACyT), México, for offering a graduate scholarship. The authors acknowledge funding from (CONACyT) México, through grants # INFR-255791-2015, INFR-226208-2014, and A1-S-26720. The authors gratefully acknowledge the Transmission Electron Microscope Laboratory of the University of Sonora, for extending TEM facilities utilized in this work.

REFERENCES

- (1) Bondar, N. V.; Brodyn, M. S. Evolution of Excitonic States in Two-Phase Systems with Quantum Dots of II-VI Semiconductors near the Percolation Threshold. *Phys. E* **2010**, *42*, 1549–1554.
- (2) Yu, Y.; Xu, L.; Chen, J.; Gao, H.; Wang, S.; Fang, J.; Xu, S. Hydrothermal Synthesis of GSH-TGA Co-Capped CdTe Quantum Dots and Their Application in Labeling Colorectal Cancer Cells. *Colloids Surf., B* **2012**, *95*, 247–253.
- (3) Li, H.; Shih, W. Y.; Shih, W.-H. Non-Heavy-Metal ZnS Quantum Dots with Bright Blue Photoluminescence by a One-Step Aqueous Synthesis. *Nanotechnology* **2007**, *18*, 205604.
- (4) Özgür, Ü.; Alivov, Y. I.; Liu, C.; Teke, A.; Reshchikov, M. A.; Dogan, S.; Avrutin, V.; Cho, S. J.; Morkoc, H. A Comprehensive Review of ZnO Materials and Devices. *J. Appl. Phys.* **2005**, *98*, 041301.
- (5) Rohlfiing, M.; Krüger, P.; Pollmann, J. Role of Semicore Electrons in Quasiparticle Band-Structure Calculations. *Phys. Rev. B: Condens. Matter Mater. Phys.* **1998**, *57*, 6485–6492.
- (6) Su, G.; Liu, C.; Deng, Z.; Zhao, X.; Zhou, X. Size-Dependent Photoluminescence of PbS QDs Embedded in Silicate Glasses. *Opt. Mater. Express* **2017**, *7*, 2194–2207.
- (7) Seo, Y.-S.; Justin Raj, C.; Kim, D.-J.; Chul Kim, B.; Yu, K.-H. Effect of CdSe/ZnS Quantum Dots Dispersion in Silicone Based Polymeric Fluids. *Mater. Lett.* **2014**, *130*, 43–47.
- (8) Sookhakian, M.; Amin, Y. M.; Basirun, W. J.; Tajabadi, M. T.; Kamarulzaman, N. Synthesis, Structural, and Optical Properties of Type-II ZnO-ZnS Core-Shell Nanostructure. *J. Lumin.* **2014**, *145*, 244–252.
- (9) Naughton, M. S.; Kumar, V.; Bonita, Y.; Deshpande, K.; Kenis, P. J. A. High Temperature Continuous Flow Synthesis of CdSe/CdS/ZnS, CdS/ZnS, and CdSeS/ZnS Nanocrystals. *Nanoscale* **2015**, *7*, 15895–15903.

(10) Chistyakov, A. A.; Zvaigzne, M. A.; Nikitenko, V. R.; Tameev, A. R.; Martynov, I. L.; Prezhdo, O. V. Optoelectronic Properties of Semiconductor Quantum Dot Solids for Photovoltaic Applications. *J. Phys. Chem. Lett.* **2017**, *8*, 4129–4139.

(11) Zazueta-Raynaud, A.; Lopez-Delgado, R.; Pelayo-Ceja, J. E.; Alvarez-Ramos, M. E.; Ayon, A. Utilization of Down-Shifting Photoluminescent ZnO Quantum Dots on Solar Cells. *Mater. Res. Express* **2017**, *4*, 076203.

(12) Lopez-Delgado, R.; Higuera-Valenzuela, H. J.; Zazueta-Raynaud, A.; Ramos-Carrasco, A.; Pelayo, J. E.; Berman-Mendoza, D.; Álvarez-Ramos, M. E.; Ayon, A. Solar Cell Efficiency Improvement Employing Down-Shifting Silicon Quantum Dots. *Microsyst. Technol.* **2018**, *24*, 495–502.

(13) Lopez-Delgado, R.; Zhou, Y.; Zazueta-Raynaud, A.; Zhao, H.; Pelayo, J. E.; Vomiero, A.; Álvarez-Ramos, M. E.; Rosei, F.; Ayon, A. Enhanced Conversion Efficiency in Si Solar Cells Employing Photoluminescent Down-Shifting CdSe/CdS Core/Shell Quantum Dots. *Sci. Rep.* **2017**, *7*, 14104.

(14) Kamat, P. V. Quantum Dot Solar Cells. The next Big Thing in Photovoltaics. *J. Phys. Chem. Lett.* **2013**, *4*, 908–918.

(15) Janssen, R. A. J.; Stouwdam, J. W. Red, Green, and Blue Quantum Dot LEDs with Solution Processable ZnO Nanocrystal Electron Injection Layers. *J. Mater. Chem.* **2008**, *18*, 1889.

(16) Minot, E. D.; Kelkensberg, F.; Van Kouwen, M.; Van Dam, J. A.; Kouwenhoven, L. P.; Zwiller, V.; Borgström, M. T.; Wunnicke, O.; Verheijen, M. A.; Bakkers, E. P. A. M. Single Quantum Dot Nanowire LEDs. *Nano Lett.* **2007**, *7*, 367–371.

(17) Liu, Y.-Q.; Zhang, D.-D.; Wei, H.-X.; Ou, Q.-D.; Li, Y.-Q.; Tang, J.-X. Highly Efficient Quantum-Dot Light Emitting Diodes with Sol-Gel ZnO Electron Contact. *Opt. Mater. Express* **2017**, *7*, 2161–2167.

(18) Zhang, Q.; Nie, C.; Chang, C.; Guo, C.; Jin, X.; Qin, Y.; Li, F.; Li, Q. Highly Luminescent Red Emitting CdZnSe/ZnSe Quantum Dots Synthesis and Application for Quantum Dot Light Emitting Diodes. *Opt. Mater. Express* **2017**, *7*, 3875–3884.

(19) Shen, H.; Bai, X.; Wang, A.; Wang, H.; Qian, L.; Yang, Y.; Titov, A.; Hyvonen, J.; Zheng, Y.; Li, L. S. High-Efficient Deep-Blue Light-Emitting Diodes by Using High Quality ZnxCd1-XS/ZnS Core/Shell Quantum Dots. *Adv. Funct. Mater.* **2014**, *24*, 2367–2373.

(20) Jin, X.; Bai, J.; Gu, X.; Chang, C.; Shen, H.; Zhang, Q.; Li, F.; Chen, Z.; Li, Q. Efficient Light-Emitting Diodes Based on Reverse Type-I Quantum Dots. *Opt. Mater. Express* **2017**, *7*, 4395–4407.

(21) Caruge, J. M.; Halpert, J. E.; Wood, V.; Bulović, V.; Bawendi, M. G. Colloidal Quantum-Dot Light-Emitting Diodes with Metal-Oxide Charge Transport Layers. *Nat. Photonics* **2008**, *2*, 247–250.

(22) Chukwuocha, E. O.; Onyeaju, M. C.; Harry, T. S. T. Theoretical Studies on the Effect of Confinement on Quantum Dots Using the Brus Equation. *World J. Condens. Matter Phys.* **2012**, *02*, 96–100.

(23) Poornaprakash, B.; Amaranatha Reddy, D.; Murali, G.; Madhusudhana Rao, N.; Vijayalakshmi, R. P.; Reddy, B. K. Composition Dependent Room Temperature Ferromagnetism and PL Intensity of Cobalt Doped ZnS Nanoparticles. *J. Alloys Compd.* **2013**, *577*, 79–85.

(24) Virpal; Kumar, J.; Thangaraj, R.; Sharma, S.; Singh, R. C. Enhanced Dielectric Permittivity and Photoluminescence in Cr Doped ZnS Nanoparticles. *Appl. Surf. Sci.* **2017**, *416*, 296–301.

(25) Tripathi, L. N.; Mishra, C. P.; Chaubey, B. R. Luminescence in ZnS: La and ZnS: (Mn, La) Phosphors. *Pramana* **1982**, *19*, 385–398.

(26) Caldiño, U.; Alvarez, E.; Speghini, A.; Bettinelli, M. Cold and Warm White Light Generation Using Zn(PO₃)₂ Glasses Activated by Ce³⁺, Dy³⁺ and Mn²⁺. *J. Lumin.* **2012**, *132*, 2077–2081.

(27) Yuan, X.; Zheng, J.; Zeng, R.; Jing, P.; Ji, W.; Zhao, J.; Yang, W.; Li, H. Thermal Stability of Mn²⁺ Ion Luminescence in Mn-Doped Core-Shell Quantum Dots. *Nanoscale* **2014**, *6*, 300–307.

(28) Pal, P. P.; Manam, J. Enhanced Luminescence of ZnO:RE³⁺ (RE=Eu, Tb) Nanorods by Li⁺ Doping and Calculations of Kinetic Parameters. *J. Lumin.* **2014**, *145*, 340–350.

- (29) Jadwisienczak, W. M.; Lozykowski, H. J.; Xu, a.; Patel, B. Visible Emission from ZnO Doped with Rare-Earth Ions. *J. Electron. Mater.* **2002**, *31*, 776–784.
- (30) Haque, N.; Hughes, A.; Lim, S.; Vernon, C. Rare Earth Elements: Overview of Mining, Mineralogy, Uses, Sustainability and Environmental Impact. *Resources* **2014**, *3*, 614–635.
- (31) Zhang, W.-J.; Pan, C.-Y.; Cao, F.; Yang, X. White-Light-Emitting Cu,Mn Co-Doped Zn-In-S/ZnS Quantum Dots with High Stability and Their Electroluminescence. *J. Mater. Chem. C* **2017**, *5*, 10533–10542.
- (32) Wang, C.; Xu, S.; Wang, Y.; Wang, Z.; Cui, Y. Aqueous Synthesis of Multilayer Mn:ZnSe/Cu:ZnS Quantum Dots with White Light Emission. *J. Mater. Chem. C* **2014**, *2*, 660–666.
- (33) Saavedra Rodríguez, G.; Carrillo Torres, R. C.; Sánchez Zeferino, R.; Alvarez Ramos, M. E. Stabilized Blue Emitting ZnS@SiO₂ Quantum Dots. *Opt. Mater.* **2019**, *89*, 396–401.
- (34) Fang, X.; Zhai, T.; Gautam, U. K.; Li, L.; Wu, L.; Bando, Y.; Golberg, D. ZnS Nanostructures: From Synthesis to Applications. *Prog. Mater. Sci.* **2011**, *56*, 175–287.
- (35) Joicy, S.; Saravanan, R.; Prabhu, D.; Ponpandian, N.; Thangadurai, P. Mn²⁺ Ion Influenced Optical and Photocatalytic Behaviour of Mn–ZnS Quantum Dots Prepared by a Microwave Assisted Technique. *RSC Adv.* **2014**, *4*, 44592–44599.
- (36) Tian, Y.; Zhao, Y.; Tang, H.; Zhou, W.; Wang, L.; Zhang, J. Synthesis of ZnS Ultrathin Nanowires and Photoluminescence with Mn²⁺-doping. *Mater. Lett.* **2015**, *148*, 151–154.
- (37) Bian, W.; Ma, J.; Liu, Q.; Wei, Y.; Li, Y.; Dong, C.; Shuang, S. A Novel Phosphorescence Sensor for Co²⁺ Ion Based on Mn-Doped ZnS Quantum Dots. *Luminescence* **2013**, *29*, 151–157.
- (38) Velikov, K. P.; Van Blaaderen, A. Synthesis and Characterization of Monodisperse Core-Shell Colloidal Spheres of Zinc Sulfide and Silica. *Langmuir* **2001**, *17*, 4779–4786.
- (39) Zhao, J. G.; Zhang, H. H. Hydrothermal Synthesis and Characterization of ZnS Hierarchical Microspheres. *Superlattices Nanostruct.* **2012**, *51*, 663–667.
- (40) Motlan; Zhu, G.; Drozdowicz-Tomsia, K.; McBean, K.; Phillips, M. R.; Goldys, E. M. Annealing of ZnS Nanocrystals Grown by Colloidal Synthesis. *Opt. Mater.* **2007**, *29*, 1579–1583.
- (41) Shahi, A. K.; Pandey, B. K.; Singh, B. P.; Gupta, B. K.; Singh, S.; Gopal, R. Photo Physical Studies of PVP Arrested ZnS Quantum Dots. *Electron. Mater. Lett.* **2017**, *13*, 160–167.
- (42) Dalpian, G. M.; Chelikowsky, J. R. Self-Purification in Semiconductor Nanocrystals. *Phys. Rev. Lett.* **2006**, *96*, 226802.
- (43) Mocatta, D.; Cohen, G.; Schattner, J.; Millo, O.; Rabani, E.; Banin, U. Heavily Doped Semiconductor Nanocrystal Quantum Dots. *Science* **2011**, *332*, 77–81.
- (44) Pathak, C. S.; Mandal, M. K.; Agarwala, V. Optical Properties of Undoped and Cobalt Doped ZnS Nanophosphor. *Mater. Sci. Semicond. Process.* **2013**, *16*, 467–471.
- (45) Poornaprakash, B.; Poojitha, P. T.; Chalapathi, U.; Subramanyam, K.; Park, S.-H. Synthesis, Structural, Optical, and Magnetic Properties of Co Doped, Sm Doped and Co+Sm Co-Doped ZnS Nanoparticles. *Phys. E* **2016**, *83*, 180–185.
- (46) Yang, P.; Lü, M.; Zhou, G.; Yuan, D.; Xu, D. Photoluminescence Characteristics of ZnS Nanocrystallites Co-Doped with Co²⁺ and Cu²⁺. *Inorg. Chem. Commun.* **2001**, *4*, 734–737.
- (47) Langford, J. I.; Wilson, A. J. C. Scherrer after Sixty Years: A Survey and Some New Results in the Determination of Crystallite Size. *J. Appl. Crystallogr.* **1978**, *11*, 102–113.
- (48) Khorsand Zak, A.; Majid, W. H. A.; Abrishami, M. E.; Yousefi, R. X-Ray Analysis of ZnO Nanoparticles by Williamson-Hall and Size-Strain Plot Methods. *Solid State Sci.* **2011**, *13*, 251–256.
- (49) Van De Walle, C. G.; Laks, D. B.; Neumark, G. F.; Pantelides, S. T. First-Principles Calculations of Solubilities and Doping Limits: Li, Na, and N in ZnSe. *Phys. Rev. B* **1993**, *47*, 9425–9434.
- (50) Chan, T.-L.; Tiago, M. L.; Kaxiras, E.; Chelikowsky, J. R. Size Limits on Doping Phosphorus into Silicon Nanocrystals. *Nano Lett.* **2008**, *8*, 596–600.
- (51) Brafman, O.; Mitra, S. S. Raman Effect in Wurtzite- and Zinc-Blende-Type ZnS Single Crystals. *Phys. Rev.* **1968**, *171*, 931–934.
- (52) Serrano, J.; Cantarero, A.; Cardona, M.; Garro, N.; Lauck, R.; Tallman, R. E.; Ritter, T. M.; Weinstein, B. A. Raman Scattering in β -ZnS. *Phys. Rev. B: Condens. Matter Mater. Phys.* **2004**, *69*, 014301.
- (53) Trajić, J.; Kostić, R.; Romčević, N.; Romčević, M.; Mitrić, M.; Lazović, V.; Balaž, P.; Stojanović, D. Raman Spectroscopy of ZnS Quantum Dots. *J. Alloys Compd.* **2015**, *637*, 401–406.
- (54) Kornienko, N.; Resasco, J.; Becknell, N.; Jiang, C.-M.; Liu, Y.-S.; Nie, K.; Sun, X.; Guo, J.; Leone, S. R.; Yang, P. Operando Spectroscopic Analysis of an Amorphous Cobalt Sulfide Hydrogen Evolution Electrocatalyst. *J. Am. Chem. Soc.* **2015**, *137*, 7448–7455.
- (55) Morales, A. E.; Mora, E. S.; Pal, U. Use of Diffuse Reflectance Spectroscopy for Optical Characterization of Un-Supported Nanostructures. *Rev. Mex. Fis. S* **2007**, *53*, 18–22.
- (56) Taran, M. N.; Koch-Muller, M.; Feenstra, A. Optical Spectroscopic Study of Tetrahedrally Coordinated Co²⁺ in Natural Spinel and Staurolite at Different Temperatures and Pressures. *Am. Mineral.* **2009**, *94*, 1647–1652.
- (57) Wood, D. L.; Remeika, J. P. Optical Absorption of Tetrahedral Co³⁺ and Co²⁺ in Garnets. *J. Chem. Phys.* **1967**, *46*, 3595–3602.
- (58) Alonso, P. J.; Alcalá, R. On the Optical Absorption Spectrum of Co²⁺ in CaF₂. *Phys. Status Solidi A* **1977**, *81*, 333–339.
- (59) Wei, L.; Li, Z.; Zhang, W. F. Influence of Co Doping Content on Its Valence State in Zn_{1-x}Co_xO (0 < x < 0.15) Thin Films. *Appl. Surf. Sci.* **2009**, *255*, 4992–4995.
- (60) Peng, L.; Wang, Y. Effects of the Template Composition and Coating on the Photoluminescence Properties of ZnS:Mn Nanoparticles. *Nanoscale Res. Lett.* **2010**, *5*, 839–845.
- (61) Lu, S. W.; Lee, B. I.; Lin, Z.; Tong, W.; Wagner, B. K.; Park, W.; Summers, C. J. Synthesis and Photoluminescence Enhancement of Mn²⁺-Doped ZnS Nanocrystals. *J. Lumin.* **2000**, *92*, 73–78.
- (62) Yamamoto, H.; McClure, D. S.; Marzocco, C.; Waldman, M. Energy Migration In a Nearly One-Dimensional Compound, Tetramethyl Ammonium Manganese Chloride (TMMC). *Chem. Phys.* **1977**, *22*, 79–87.
- (63) Yuan, X.; Ma, R.; Zhang, W.; Hua, J.; Meng, X.; Zhong, X.; Zhang, J.; Zhao, J.; Li, H. Dual Emissive Manganese and Copper Co-Doped Zn – In – S Quantum Dots as a Single Color-Converter for High Color Rendering White- Light-Emitting Diodes. *ACS Appl. Mater. Interfaces* **2015**, *7*, 8659–8666.
- (64) Alvarez-Ramos, M. E.; Alvarado-Rivera, J.; Zayas, M. E.; Caldiño, U.; Hernández-Paredes, J. Yellow to Orange-Reddish Glass Phosphors: Sm³⁺, Tb³⁺ and Sm³⁺/Tb³⁺ in Zinc Tellurite-Germanate Glasses. *Opt. Mater.* **2018**, *75*, 88–93.
- (65) Carrillo-Torres, R. C.; Saavedra-Rodríguez, G.; Alvarado-Rivera, J.; Caldiño, U.; Sánchez-Zeferino, R.; Alvarez-Ramos, M. E. Tunable Emission and Energy Transfer in TeO₂-GeO₂-ZnO and TeO₂-GeO₂-MgCl₂ Glasses Activated with Eu³⁺/Dy³⁺ for Solid State Lighting Applications. *J. Lumin.* **2019**, *212*, 116–125.
- (66) Inokuti, M.; Hirayama, F. Influence of Energy Transfer by the Exchange Mechanism on Donor Luminescence. *J. Chem. Phys.* **1965**, *43*, 1978–1989.